PASJ: Publ. Astron. Soc. Japan **57**, 995–1007, 2005 December 25

Three-Dimensional Magnetohydrodynamic Simulation of Nonlinear Magnetic Buoyancy Instability of Flux Sheets with Magnetic Shear

Satoshi NOZAWA
Department of Science, Ibaraki University, 2-1-1 Bunkyo, Mito, Ibaraki 310-8512
snozawa@env.sci.ibaraki.ac.jp

(Received 2005 April 20; accepted 2005 September 9)

Abstract

A series of three-dimensional magnetohydrodynamic simulations is used to study the nonlinear evolution of the magnetic buoyancy instability of a magnetic flux sheet with magnetic shear. A horizontal flux sheet that is initially placed below the solar photosphere is susceptible to both the interchange instability and the Parker instability (the undular mode of the magnetic buoyancy instability). The growth rate in the linear stage of the instability in the numerical simulation is consistent with that predicted by linear theory. In the nonlinear stage, the development depends on the initial perturbation as well as the initial magnetic field configuration (i.e., the presence of magnetic shear). When an initial perturbation is assumed to be periodic, the emerging flux rises to the corona and the magnetic field expands like a potential field, as observed in 2D simulations. When an initial non-periodic perturbation or random perturbations are assumed, the magnetic flux expands horizontally when the magnetic field emerges a little into the photosphere. The distribution of the magnetic field and gas tends to be in a new state of magnetohydrostatic equilibrium. When magnetic shear is present in the initial magnetic flux sheets, the interchange mode is stabilized so that the emerging loop is higher than in the no magnetic shear case. We discuss how the presented results are related to the emerging flux observed on the Sun.

Key words: instabilities — MHD — plasmas — Sun: magnetic fields

1. Introduction

The magnetic activity observed on the Sun is caused by the emergence of magnetic flux created deep in the convection zone (see, e.g., Parker 1979). Sunspots and active regions are formed by magnetic flux tubes emerging from the interior of the Sun into the solar atmosphere (see, e.g., Zwaan 1985, 1987) as a result of magnetic buoyancy (Parker 1955). Much of the dynamics of the emerging magnetic field is not yet well understood because of its intrinsic nonlinear properties. Hence, it is important to study the nonlinear dynamics of emerging magnetic flux and magnetic buoyancy.

It has been found that a flux sheet in magnetohydrostatic equilibrium in a gravitationally stratified gas layer becomes unstable due to magnetic buoyancy. This is called the magnetic buoyancy instability (see, e.g., Hughes, Proctor 1988; Tajima, Shibata 1997). There are two modes in magnetic buoyancy instability: the undular mode ($\boldsymbol{k} \parallel \boldsymbol{B}$) and the interchange mode ($\boldsymbol{k} \perp \boldsymbol{B}$), where $\boldsymbol{k}$ is the wavenumber vector and $\boldsymbol{B}$ is the magnetic field vector. The undular mode is often called the Parker instability (Parker 1966) in astrophysical literature and the interchange mode is sometimes called the flute instability or the magnetic Rayleigh–Taylor instability (Kruskal, Schwarzchild 1954). The undular mode occurs for long-wavelength perturbations along the magnetic field lines, when the magnetic buoyancy created by gas traveling down along a field line is greater than the restoring magnetic tension. On the other hand, the interchange mode occurs for short-wavelength perturbations, when the interchange of two straight flux tubes reduces the potential energy in the system. The linear growth rate of the interchange mode is generally much greater than that of the undular mode because of the short wavelength, though the nonlinear stage is dominated by the undular mode in many cases (Matsumoto et al. 1993; Tajima, Shibata 1997). Hence, the undular mode (hereafter, called the Parker instability) is more important than the interchange mode in nonlinear problems, and therefore in astrophysical problems.

The first published nonlinear simulation of the Parker instability was done by Baierlein (1983), although the calculation was one dimensional. Nonlinear two-dimensional (2D) magnetohydrodynamic (MHD) simulations of the Parker instability were first made by Matsumoto et al. (1988). They found that giant interstellar clouds are formed in the nonlinear stage of the Parker instability and that a shock wave is formed within the flow of the cloud along a rising loop. Applying the simulations of Matsumoto et al. (1988) to the solar case, Shibata et al. (1989b, 1990a) showed that self-similar expansion of a magnetic loop occurs in the nonlinear evolution of the 2D Parker instability in the solar atmosphere (i.e., in the solar emerging flux). Nozawa et al. (1992) have made an extensive study of the linear and nonlinear evolution of the Parker instability in the convectively unstable gas layer. Further 2D simulations have been made by Kamaya et al. (1996) on triggering nonlinear instability by supernova explosion and by Basu, Mouschovias, and Paleologou (1997) and Kim et al. (2000) for application to galactic disks.

As shown by Parker's (1966) original analysis, however, the most unstable mode shows three-dimensional (3D) behavior. That is, the instability has a maximum growth rate for non-zero $k_\perp$, even when non-zero $k_\parallel$ is the main cause of the instability, where $k_\perp$ is the wavenumber vector perpendicular to the magnetic field and $k_\parallel$ is the wavenumber vector parallel

to the magnetic field. Thus, 3D nonlinear simulations are necessary to examine the true nonlinear evolution of the Parker instability in 3D space. Matsumoto and Shibata (1992) and Matsumoto et al. (1993) first reported 3D nonlinear simulations of the Parker instability for both the solar and galactic cases and confirmed the basic results of the previous 2D simulations regarding, for example, cloud formation, shock waves and self-similar evolution. However, the spatial and temporal scales of these studies depended on $k_\perp$. If a large $k_\perp$ is initially assumed, the magnetic loop tends to have a thinner structure and suffers from horizontal expansion, which eventually suppress the upward expansion (Matsumoto et al. 1993). Similar thin structures have been found in more recent 3D simulations (Kim et al. 1998, 2001, 2002; Hanasz et al. 2002).

If magnetic shear is present in the initial magnetized gas layer, the interchange mode is stabilized, i.e., the growth of thin structures is suppressed and larger scale structures may appear (Hanawa et al. 1992). Kusano, Moriyama, and Miyoshi (1998) using 2.5D MHD simulations showed that larger scale structures are created in the presence of magnetic shear. Such magnetic shear is often observed in solar active regions as twisted flux tubes (Kurokawa 1989; Ishii et al. 1998; Matsumoto et al. 1998; Fan 2001; Magara, Longcope 2001, 2003; Kurokawa et al. 2002; Ryu et al. 2003; Magara 2004; Fan, Gibson 2004) and may be created in the convection zone (Cattaneo et al. 1990; Matthews et al. 1995) and under the influence of the Coriolis force (Shibata, Matsumoto 1991; Chou et al. 1999; Hanasz et al. 2002). Nevertheless, no one has yet studied the effect of magnetic shear on the 3D nonlinear evolution of the Parker instability.

In this paper, by using 3D MHD simulations, we present a detailed analysis of the 3D nonlinear evolution of the Parker instability in a magnetic flux sheet with *magnetic shear* and examine the effects of magnetic shear on the nonlinear Parker instability. The initial gas layer and magnetic field are assumed to be suitable for application to a solar emerging flux (see, e.g., Shibata et al. 1989a), though the basic physics is also applicable to the galactic case. Section 2 details the assumptions, basic equations, and numerical procedures of the study. The numerical results are described in section 3, and section 4 is devoted to discussion and conclusions.

2. Method of Numerical Simulation

2.1. Assumptions and Basic Equations

The assumptions, basic equations, and initial conditions are similar to those in Nozawa et al. (1992). That is, we assume the following: (1) the medium is an ideal MHD plasma, (2) the gas is a polytrope of index $\gamma = 1.05$, (3) the magnetic field is frozen into the gas, and (4) the viscosity and resistivity are neglected.

Cartesian coordinates (x, y, z) are adopted, such that the z-direction is anti-parallel to the gravitational acceleration vector. The gravitational acceleration is assumed to be constant. Thus, the basic equations in vector form are as follows:

$$\frac{\partial \rho}{\partial t} + \nabla \cdot (\rho \boldsymbol{V}) = 0, \tag{1}$$

$$\frac{\partial}{\partial t}(\rho \boldsymbol{V}) + \nabla \cdot \left(\rho \boldsymbol{V}\boldsymbol{V} + p\boldsymbol{I} - \frac{\boldsymbol{B}\boldsymbol{B}}{4\pi} + \frac{\boldsymbol{B}^2}{8\pi}\boldsymbol{I} \right) - \rho \boldsymbol{g} = 0, \tag{2}$$

$$\frac{\partial}{\partial t}\left(\rho U + \frac{1}{2}\rho \boldsymbol{V}^2 + \frac{\boldsymbol{B}^2}{8\pi} \right) + \nabla \cdot \left[\left(\rho U + p + \frac{1}{2}\rho \boldsymbol{V}^2 \right) \boldsymbol{V} + \frac{c}{4\pi}\boldsymbol{E} \times \boldsymbol{B} \right] - \rho \boldsymbol{g} \cdot \boldsymbol{V} = 0, \tag{3}$$

$$\frac{\partial \boldsymbol{B}}{\partial t} - \nabla \times (\boldsymbol{V} \times \boldsymbol{B}) = 0, \tag{4}$$

$$U = \frac{1}{\gamma - 1}\frac{p}{\rho}, \tag{5}$$

and

$$\boldsymbol{E} = -\frac{1}{c}\boldsymbol{V} \times \boldsymbol{B}, \tag{6}$$

where ρ is the density, $\boldsymbol{V} = (V_x, V_y, V_z)$ the velocity vector, p the thermal pressure, t the time, $\boldsymbol{g} = (0, 0, -g)$ the gravitational acceleration, c the velocity of light, $\boldsymbol{I}$ the unit tensor, U the internal energy, $\boldsymbol{B} = (B_x, B_y, B_z)$ the magnetic vector, $\boldsymbol{E}$ the electric field, and the other symbols have their usual meanings.

2.2. Initial Conditions and Parameters

In the simulations, the units of length, velocity, and time are H, C_s and $H/C_s \equiv \tau_0$, respectively, where C_s and H are the sound velocity and pressure scale height in the photosphere/chromosphere. It should be noted that the photospheric temperature, T_{ph} can be calculated from C_s, since $T_{ph} = \mu C_s^2/(\gamma R_g)$, where μ and R_g are the mean molecular weight and gas constant, respectively. Hence, we need not specify the value of T_{ph} explicitly. The units for gas pressure, density, and magnetic field strength are $p_0 \equiv \rho_0 C_s^2$, ρ_0 (the initial density at the base of the gas layer, $z = z_{min}$), and $B_0 \equiv \sqrt{(\rho_0 C_s^2)}$, respectively. When the numerical results are compared with observations, we use $H = 200\,\mathrm{km}$, $C_s = 10\,\mathrm{km\,s^{-1}}$, and $\tau_0 = H/C_s = 20\,\mathrm{s}$, which are typical values for the solar photosphere and chromosphere. In this case, $B_0 \simeq 500\,\mathrm{G}$, assuming $\rho_0 = 2.5 \times 10^{-7}\,\mathrm{g\,cm^{-3}}$. However, we note that our results are valid for any values of C_s, H, and ρ_0, because our model is non-dimensional and scale-free.

2.3. Unperturbed State (Initial Conditions)

We consider that the initial state is in magnetohydrostatic equilibrium. The gas layer is initially composed of three regions (see figure 1): a convectively stable layer representing a very simplified model of the solar photosphere/chromosphere and corona. The temperature is nearly constant in the upper hot layer (corona) and in the lower cold layer (photosphere/chromosphere). We take the height $z = 0$ to be the base height of the photosphere; the initial distribution of temperature in the photosphere/chromosphere and the corona is then

$$T(z) = T_{ph} + \frac{1}{2}(T_{cor} - T_{ph}) \left[\tanh\left(\frac{z - z_{cor}}{w_{tr}} \right) + 1 \right], \tag{7}$$

where T_{cor} and T_{ph} are the respective temperatures in the corona and in the photosphere/chromosphere, z_{cor} the height of the base of the corona, and w_{tr} the temperature scale height in the transition region. We take $w_{tr} = 0.6H$ and $z_{cor} = 13H$ in all of our calculations.

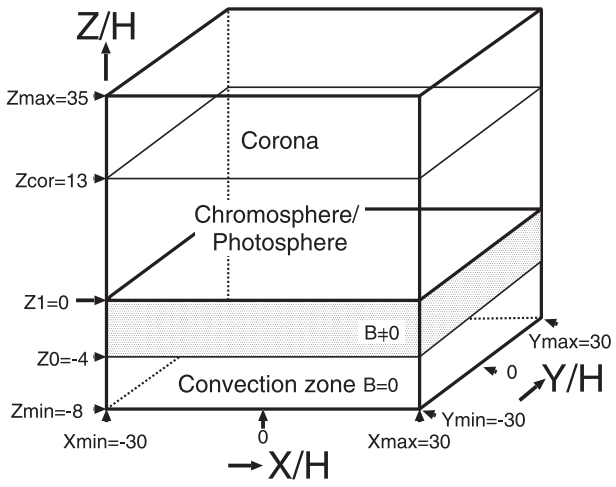

Fig. 1. Schematic depiction of the initial setup.

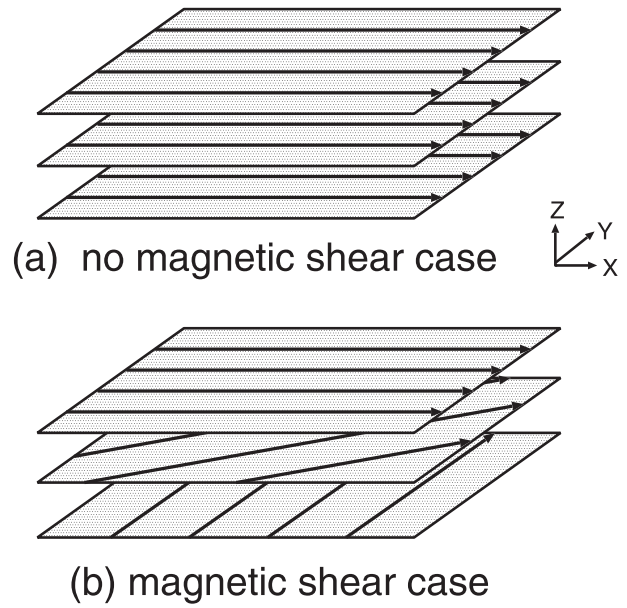

Fig. 2. Degree of magnetic shear in the magnetic sheet (a) for no magnetic shear and (b) with magnetic shear. In the upper magnetic layer, the magnetic direction is parallel to the x-direction for both cases. In the lower magnetic layer, it is parallel to the y-direction ($\theta_{00} = \pi/2$) for the case with shear.

We assume that the magnetic field is initially horizontal, $\boldsymbol{B} = [B_x(z), B_y(z), 0]$, and is localized under the photosphere. The initial density and pressure distributions are calculated numerically using the equation of magnetohydrostatic pressure balance:

$$\frac{d}{dz}\left[p + \frac{B_x^2(z) + B_y^2(z)}{8\pi}\right] + \rho g = 0, \tag{8}$$

where

$$B_x(z) = \left[\sqrt{\frac{8\pi p(z)}{\beta(z)}}\right]\cos\theta(z), \tag{9}$$

$$B_y(z) = \left[\sqrt{\frac{8\pi p(z)}{\beta(z)}}\right]\sin\theta(z), \tag{10}$$

and the plasma β is the ratio of gas pressure to magnetic pressure, with

$$\beta(z) = \beta_*/f(z), \tag{11}$$

where

$$f(z) = \left[1 + \tanh\left(\frac{z - z_0}{w_0}\right)\right]\left[1 - \tanh\left(\frac{z - z_1}{w_1}\right)\right]\Big/4. \tag{12}$$

Here β_* is β at the center of the magnetic flux sheet, z_0 and $z_1 = z_0 + D$ are the heights of the lower and upper boundaries of the magnetic flux sheet, and D is the vertical thickness of the magnetic flux sheet. We use $D = 4H \simeq 800\,\mathrm{km}$ and $w_0 = w_1 = 0.5H$ for all of our calculations and take β to be nearly constant inside the flux sheet ($z_0 \le z \le z_1$). The magnetic field direction, $\theta(z)$, is given by

$$\theta(z) = \theta_{00}\,\pi(z_1 - z)/D, \tag{13}$$

when $z_0 \le z \le z_1$, $\theta_{00} \ge \theta(z) \ge 0$. Figure 2b shows that the magnetic field lines at each height have different horizontal directions.

The free parameters are β_*, $z_{\min}$ (depth of the convection zone), and z_0 (base height of the flux sheet). We will use $\beta_* = 1$, $z_{\min} = -8H \simeq -1600\,\mathrm{km}$, and $z_0 = -4H \simeq -800\,\mathrm{km}$. Although these values are not realistic for the actual solar convection zone (see, e.g., Spruit 1974; Spruit et al. 1990), they are acceptable for our first attempt to study the fundamental nonlinear interaction between the magnetic field and convection just below the photosphere.

The initial temperature, T, density, ρ, gas pressure, p, and magnetic field strength, $|\boldsymbol{B}|$, distributions for our base model ($z_{\min} = -8H$, $z_0 = -4H$, $\beta_* = 1$) are shown in figure 3.

2.4. Boundary Conditions

We assumed rigid walls at $z = z_{\min}$ and $z = z_{\max}$ and periodic boundaries at $x = x_{\min}$, $y = y_{\min}$ and $x = x_{\max}$, $y = y_{\max}$, respectively. The rigid wall is the simplest and most reliable condition to implement at $z = z_{\min}$ in the high-energy density region of the convection zone. The difficulties are particularly acute here, since the density ratio between the convection zone and the corona is $\sim 10^{-7}$, so that small errors generated at the free boundary at $z = z_{\min}$ are enormously amplified by the steep density gradient in the photosphere and chromosphere as they propagate from the convection zone into the corona. The effect of the rigid boundary at $z = z_{\max}$ is small, since the energy density is smallest in the computational box.

2.5. Numerical Method

Non-dimensional MHD equations (1)–(6) are solved numerically by using a modified Lax–Wendroff scheme (Rubin, Burstein 1967) with artificial viscosity (Ritchmyer, Morton 1967), as in previous studies (e.g., Shibata 1983; Matsumoto et al. 1988, 1993, 1998; Shibata et al. 1989a, 1989b, 1990b; Nozawa et al. 1992)

The magnetohydrostatic gas layer shown above is unstable for the interchange and Parker instabilities. In order to instigate

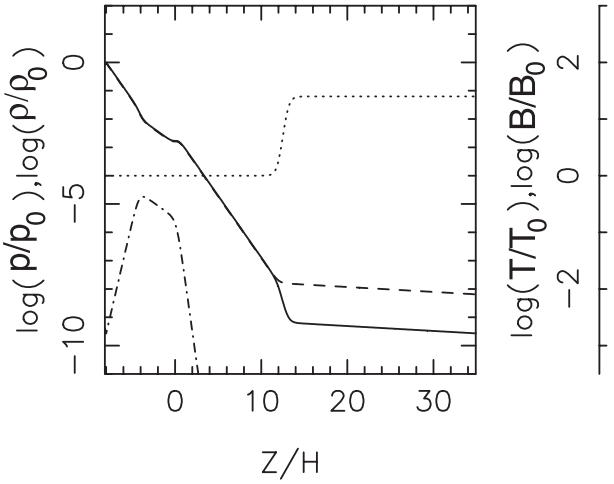

Fig. 3. One-dimensional (z-) distribution of the initial density (solid curve), pressure (dashed curve), magnetic field strength (dash-dotted curve), and temperature (dotted curve). ρ_0, p_0, T_0, and B_0 denote the initial density, pressure, temperature, and magnetic field strength at $z = z_{\min}$ ($z = -8H$), respectively.

instability, small velocity perturbations of the form

$$V_z = f(z) A C_s \cos\left(\frac{2\pi x}{\lambda_x}\right) \cos\left(\frac{2\pi y}{\lambda_y}\right) \tag{14}$$

are given initially within the finite horizontal domain ($|x, y| \leq \lambda/2$), where λ is the wavelength of the small velocity perturbations. A typical case is $\lambda_x = \lambda_y$ ($k_y/k_x = 1$). Here C_s is the sound velocity in the photosphere and A ($= 10^{-3}$) is the maximum value of V_z/C_s in the initial perturbation. In the 2D case (model 1), a small velocity perturbation is used, of the form

$$V_x = f(z) A C_s \sin\left(\frac{2\pi x}{\lambda}\right) \tag{15}$$

Although the distribution of the velocity given by equation (14) is not exactly an eigenfunction, the growth rate of the perturbation in the linear regime agrees well with that obtained from an exact linear analysis, as will be discussed in the Appendix (see also Matsumoto et al. 1988; Shibata et al. 1989a).

The mesh size is $\Delta z_0 = 0.15H$ for $z \leq z_{\rm cor}$, which slowly increases up to $\Delta z_{\max} = 0.375H = T_{\rm cor}/(10 \times \Delta z_0)$ for $z \geq z_{\rm cor}$.

Table 1. Models and parameters.

Model	2D or 3D	$k_x H$ or kH	λ/H	Shear	$k_y : k_x$
1	2D	0.31	20	0.0	⋯
2	3D	0.5	12.6	0.0	1 : 1
3	3D	0.5	12.6	0.5π	1 : 1
4	3D	random	random	0.0	1 : 1
5	3D	random	random	0.5π	1 : 1
6	3D	0.5	12.6	0.0	2 : 1
7	3D	0.5	12.6	1.0π	2 : 1
8	3D	0.5	12.6	2.0π	2 : 1

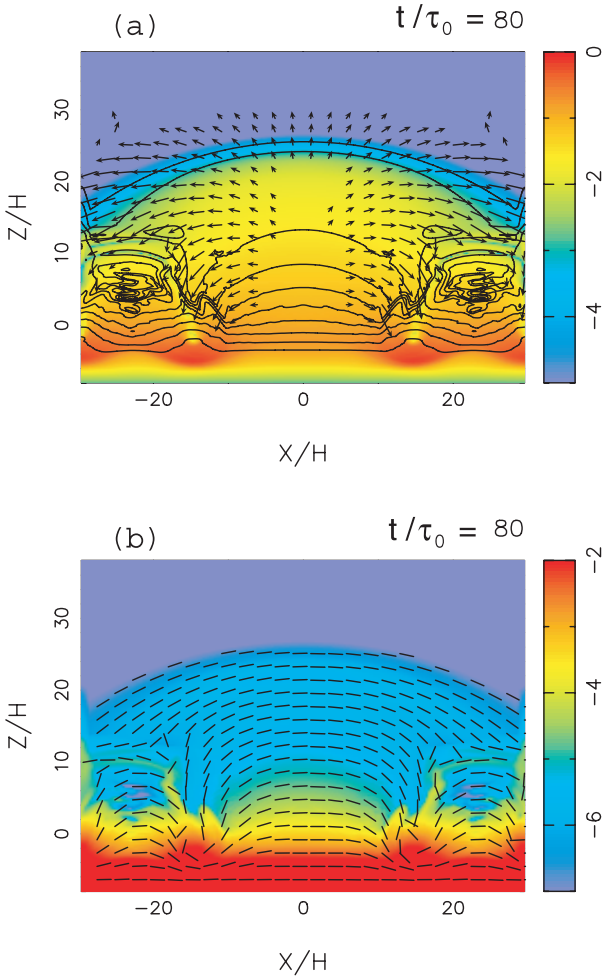

Fig. 4. 2D distributions of (a) magnetic field strength $|B| = \sqrt{B_x^2 + B_z^2}$ (colors), velocity field (vectors) and density (contour lines) and (b) magnetic field lines (lines) and density (gray scale colors) at $t/\tau_0 = 80$ for the 2D case (model 1). The velocity length $1H$ is $1\,C_s$ (sound velocity).

The other parameters are Δx, $\Delta y = 0.2$. The total number of mesh points is $N_x \times N_y \times N_z = 300 \times 300 \times 203$ and the total area is $[(x_{\max} - x_{\min}) \times (y_{\max} - y_{\min}) \times (z_{\max} - z_{\min})] = (60H \times 60H \times 43H)$. The parameters of the models considered here are summarized in table 1.

3. Nonlinear Simulation Results

3.1. 2D Case (Model 1)

Let us first discuss the typical nonlinear evolution of the Parker instability in the 2D case. Figures 4 and 5 show typical results for the no-shear mode.

All results agree with those of Shibata et al. (1989a), except for the time sequence; the time evolution of the emerging flux loop is slow, compared with that of Shibata et al. (1989a, 1989b), because the perturbation amplitude, A, is taken to be 10^{-3}. A self-similar evolution for the density (figure 5b) and magnetic field strength can be seen in figure 5d,

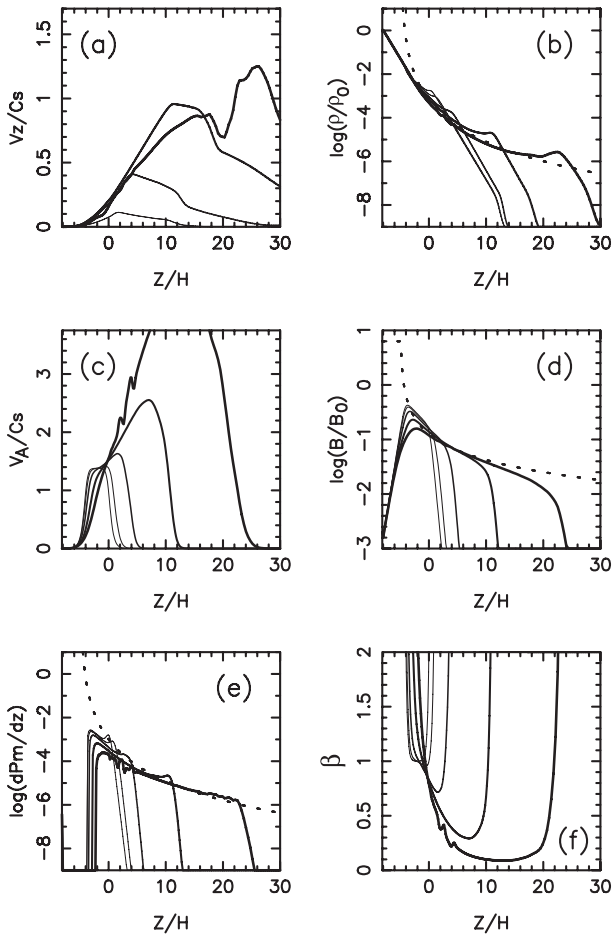

Fig. 5. z-distribution: (a) the vertical component velocity (V_z), (b) the density ($\log \rho$), (c) the local Alfvén velocity (V_A), (d) the horizontal component of the magnetic field ($\log B$), (e) the magnetic pressure [$\log(\Delta P_m/\Delta z)$], and (f) plasma β (gas pressure/magnetic pressure) at $x = 0H$ (middle of the rising loop) for model 1 (the case shown in figure 4) at $t/\tau_0 = 0$ (the thinnest line), 50, 60, 70, and 80 (the thickest line).

$$\rho \propto z^{-4} \quad \text{and} \quad B \propto z^{-1}. \tag{16}$$

In particular, the plasma β decreases to less than 0.1, which indicates that the magnetic pressure dominates over the gas pressure and the magnetic loop continues to increase (figure 5f). The dominance of the magnetic pressure leads to the formation of a current-free magnetic loop.

3.2. *No Magnetic Shear with a Localized Perturbation (Model 2)*

Let us now discuss the 3D cases. Figures 6, 7, and 8 show typical results for the no-shear mode. Figure 6c indicates that the magnetic field in the y-direction emerges from the narrow region and expands horizontally in the photosphere. The 3D displays in figure 7 show that the magnetic field lines become almost vertical in the region where the magnetic field is concentrated.

In the upper photosphere, the magnetic field is parallel to the photospheric plane and expands horizontally. Since the scale height of the photosphere is smaller than the thickness of a

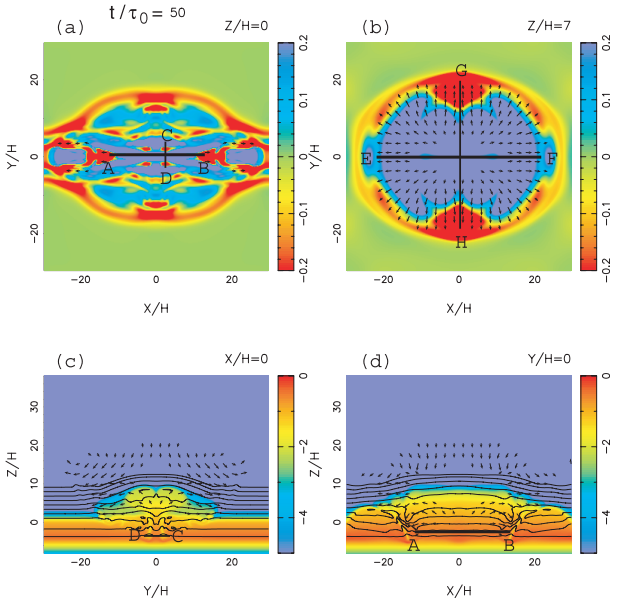

Fig. 6. Nonlinear simulation results for no magnetic shear, where an initial localized perturbation is assumed (model 2). (a) Distribution of V_z on the photosphere surface ($z = 0H$). (b) Velocity distribution in the upper photosphere ($z = 7H$). Magnetic field (colors), velocity field (vectors), and density (contour lines) on the (c) y–z surface and (d) x–z surface.

magnetic sheet, the gas pressure outside the sheet decreases rapidly. Hence, when the magnetic field slightly emerges into the photosphere, the magnetic flux expands horizontally until the magnetic pressure of the sheet is balanced with the surrounding gas pressure.

The velocity vectors also show that plasma expands in the horizontal direction more than in the vertical direction (see figures 6b, c, d). This result implies that the rise of the magnetic loop stops at lower heights ($< 10H$) and the distribution of the magnetic pressure is in a new state of magneto-hydrostatic equilibrium. The characteristic wavelength of the magnetic loop is dependent on the width 2–6H (see line C–D in figures 6a, c) in the photosphere ($z = 0$) in the y-direction. Another characteristic wavelength is the comparatively long 27–32H (line A–B in figures 6a, d), which indicates expansion of the magnetic loop in the x-direction in the photosphere ($z = 0$). However, at $z = 7H$ (the lines E–F and G–H in figure 6b), the characteristic wavelengths in both the x- and y-directions increase to 35–40H, because of the inverse cascade effect (Hachisu et al. 1992).

In figure 8a at $t/\tau_0 = 50$, 60, and 70, the top of the magnetic loop reaches $z \sim 14H$. In the last stage, the magnetic loop does not rise further. Figures 8b, d, e show the distributions of the density, magnetic field strength, and magnetic pressure, which are approximated by

$$B \propto \exp\left(-\frac{\Delta z}{H_B}\right), \qquad \rho \propto \exp\left(-\frac{\Delta z}{H_\rho}\right),$$
$$P_m \propto \exp\left(-\frac{\Delta z}{H_{P_m}}\right) \propto \exp\left(-\frac{2\Delta z}{H_B}\right), \tag{17}$$

with $H_B \sim 4.8$, $H_\rho \sim 2.4$, and $H_{P_m} \sim 2.4$. What are the

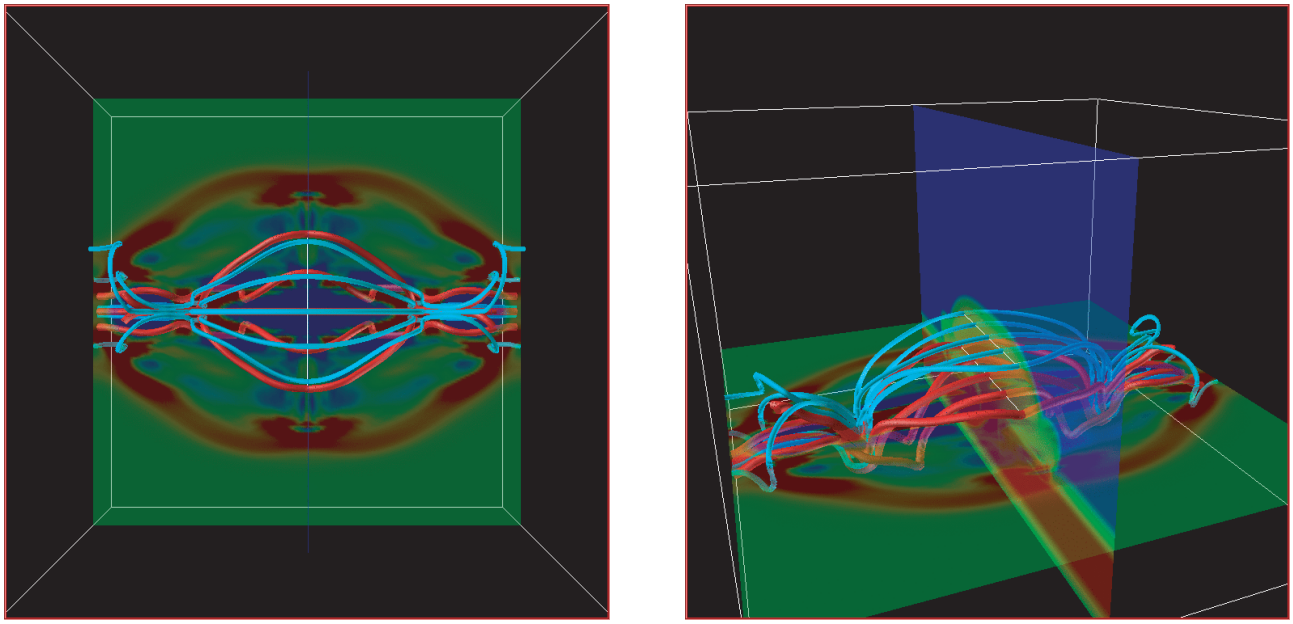

Fig. 7. Perspective view of the magnetic field at the epoch $t/\tau_0 = 55$ for no magnetic shear, where an initial sinusoidal perturbation is assumed (model 2). The five red tubes show the magnetic field lines that are connected to the points $(x, y, z) = [(-10.6H, -5.3H, 0H, 5.3H, 10.6H), 0H, 5H]$ and the five blue tubes show the magnetic field lines that are connected to $(x, y, z) = [(-8.4H, -4.2H, 0H, 4.2H, 8.4H), 0H, 14H]$.

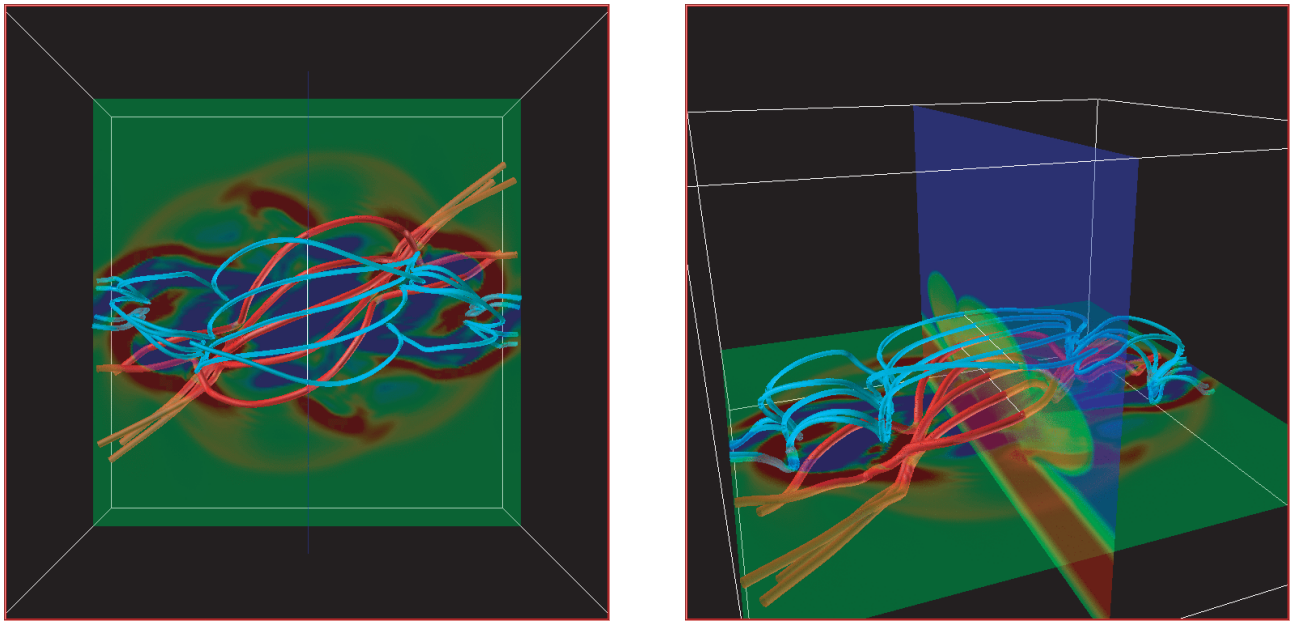

Fig. 10. Perspective view of the magnetic field at the epoch $t/\tau_0 = 55$ for the case with magnetic shear, where an initial sinusoidal perturbation is assumed (model 3).

physical meanings of these distributions? They are similar to typical distributions of the magnetic field and plasma in magnetohydrostatic equilibrium with uniform temperature and constant plasma β when the magnetic field is horizontal. In fact, an exact equilibrium solution predicts $H_\rho = (1 + 1/\beta)$ and $H_{P_m} = H_\rho$. In our simulation results, $\beta \sim 0.7$ (see figure 8f), so we have $H_\rho \sim 2.4$, which is consistent with direct simulation results. The relations $H_\rho = H_{P_m} = H_B/2$ are also consistent with magnetohydrostatic equilibrium theory.

Note that the plasma $\beta \sim 0.7$ in the rising magnetic loop is larger than that in the 2D case ($\beta \sim 0.1$). This is because the magnetic flux rapidly expands in the horizontal direction in the photosphere, so that the magnetic field becomes weak. Hence, the magnetic flux cannot expand into the corona and

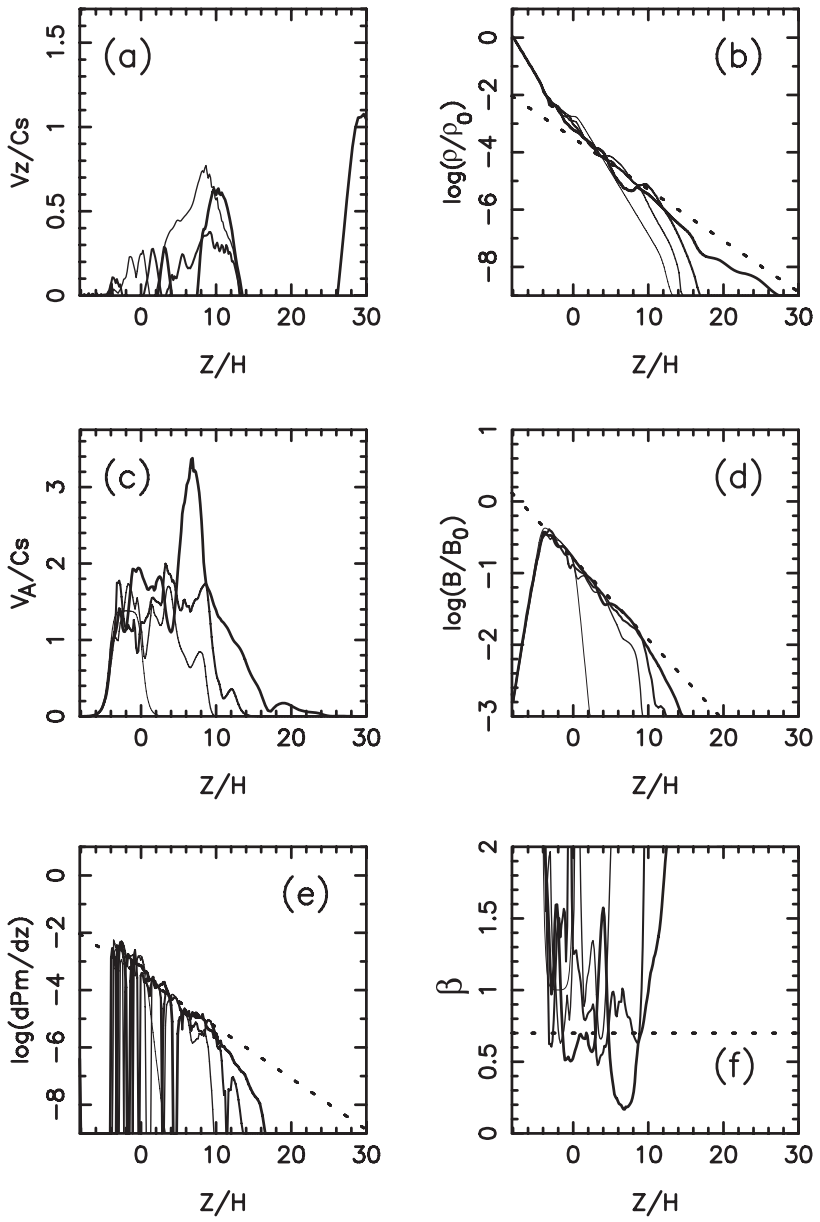

Fig. 8. z-distribution at $(x, y) = (0H, 0H)$ (middle of the rising loop) for model 2 (no-shear mode) shown in figure 6 at $t/\tau_0 = 0$, 50, 60, and 70, with all other details of the graphs being the same as in figure 5. The dashed lines in (b), (d), and (e) indicate the lines of $\rho \propto \exp(-\Delta z/H_\rho)$ with $H_\rho = 2.4$, $B \propto \exp(-\Delta z/H_B)$ with $H_B = 4.8$, and $P_{\rm m} \propto \exp(-\Delta z/H_{P_{\rm m}})$ with $H_{P_{\rm m}} = 2.4$, respectively. In (f) the dashed line is $\beta = 0.7$.

instead tends to be in magnetohydrostatic equilibrium in the photosphere and chromosphere.

3.3. Magnetic Shear with a Localized Perturbation (Model 3)

Figures 9, 10, and 11 show the results of 3D calculations for the shear mode. In figures 9a and 10, the loop that passes through the origin ($x = 0$, $y = 0$) emerges at an angle $\sim 45^\circ$ to the x-direction, while for the case of no-shear the loop is parallel to the x-direction. This is because the magnetic sheet at the depth where the field line is at 45° rises up into the photosphere at $t/\tau_0 = 50$. In the last stage of the calculation after $t/\tau_0 = 50$, a deeper magnetic sheet rises and becomes a loop with an angle greater than 45°.

Figure 9c indicates that the area where the magnetic sheet rises in the photosphere is larger than that for the no-shear case. In the shear case, the velocity vectors show that the plasma expands in the horizontal direction more than in the vertical direction (see figures 9b, c, d) and the magnetic field expands at medium heights (6–12H). Figure 9a shows that the characteristic wavelength in the x-direction is comparatively long 13H (the line A–B) and the characteristic wavelength in the 45°-direction is somewhat short 4–8H (the line C–D).

The same as in the no-shear case, the plasma density and magnetic field strength distributions in the shear mode can also be approximated by exponential functions [equation (17)] with $H_\rho \sim 2.1$, $H_B \sim 4.2$ (see figures 11b, d) and the plasma $\beta \sim 0.9$ in the magnetic loop (see figure 11f).

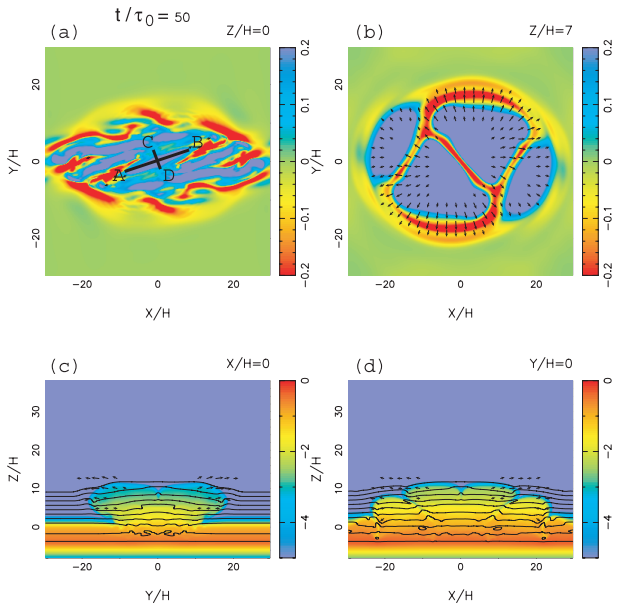

Fig. 9. Nonlinear simulation results for magnetic shear, where an initial sinusoidal perturbation is assumed (model 3). The details of the graphs are the same as in figure 6.

3.4. *Random Perturbation (Model 4 and Model 5)*

Figure 12 shows the results for a random initial perturbation for both the no-shear and shear modes. In the early stage [$\simeq t/\tau_0 = 30$ (see figures 12a,d)] the characteristic wavelength in the y-direction is small and equal to $\lambda = 3.5H$ ($\sim 60H/17$). Subsequently the wavelength increases to $\lambda = 4.6H$ ($\sim 60H/13$) at $t/\tau_0 = 40$ (see figures 12b, e) and $\lambda = 5.5H$ ($\sim 60H/11$) at $t/\tau_0 = 50$ (see figures 12c, f). In figure 13b, d, at $t/\tau_0 = 50$ the magnetic loop rises at $z = 19H$ in the no-shear case and at $z = 13H$ in the shear case. The distributions of plasma density and magnetic field are basically the same as those in previous 3D cases [equation (17)].

3.5. *Loop Height for Different Shear Cases*

Figures 14 and 15a, b, c, d show the loop height for each simulation result at $t/\tau_0 = 55$ and the maximum loop height. When $k_y/k_x < 1$, the Parker instability is easily caused, so each loop height rises comparatively high, to 15–24H at $t/\tau_0 = 55$ and over $30H$ at maximum height. On the other hand, for $k_y/k_x > 1$, the interchange instability occurs easily and the height monotonically decreases when k_y is large. When $k_y/k_x < 1$, h/L_x and h/L_y are almost 0.3–0.5, and therefore the loop expands horizontally. This is due to the stabilizing effect of magnetic shear in the interchange mode.

Figure 15e shows the plasma β for each simulation result. When the shear angle, θ_{00}, is large and k_y/k_x is small, the β value monotonically decreases (the low β regime). In particular, when $\theta_{00} > 2\pi$, the averaged plasma β is almost constant against k_y/k_x. Figures 16a, b, c show that the loop height increases and the plasma β decreases for shear angles of $\theta_{00} = 0$, π, and 2π when $k_y/k_x = 2$. When θ_{00} becomes large, the form of the emerging magnetic loop changes to a dome-like structure, because the horizontal expansion of the loop is inhibited by the magnetic shear.

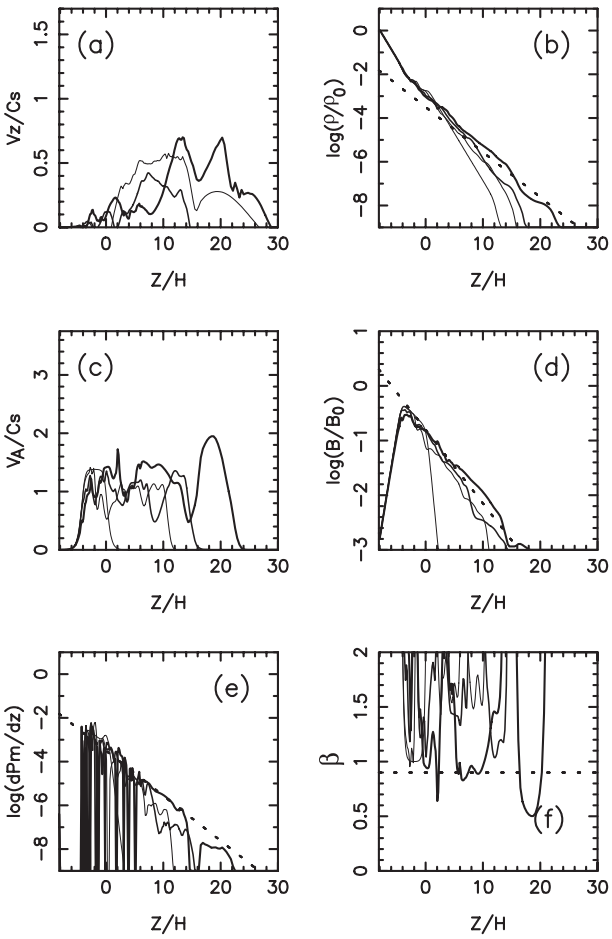

Fig. 11. z-distribution at $(x, y) = (0H, 0H)$ (middle of the rising loop) for model 3 (shear mode) shown in figure 9 at $t/\tau_0 = 0$, 50, 60, and 70. The details of the graphs are the same as in figure 8. The dashed lines in (b), (d), and (e) indicate the lines of $\rho \propto \exp(-\Delta z/H_\rho)$ with $H_\rho = 2.1$, $B \propto \exp(-\Delta z/H_B)$ with $H_B = 4.2$, and $P_{\rm m} \propto \exp(-\Delta z/H_{P_{\rm m}})$ with $H_{P_{\rm m}} = 2.1$, respectively. In (f) the dashed line is $\beta = 0.9$.

4. Summary and Discussion

4.1. *Summary*

The 3D simulations show the following:

- When the magnetic field emerges into the photosphere with a localized and random initial perturbation, the flux expands horizontally and does not go upward. At that time, the distributions of magnetic field strength, density, and pressure can be written as $\exp(-\Delta z/H_{(B,\rho,P_{\rm m})})$, as in magnetohydrostatic equilibrium, and the plasma β of the magnetic loop is 0.3–1.3 (the magnetic field strength is weak).
- The plasma β of the magnetic loop is larger (~ 0.01–0.1) than that of the 2D case. When an initial periodic perturbation is assumed, the emerging flux rises to the corona and the magnetic field expands like a potential field as in the typical 2D case.

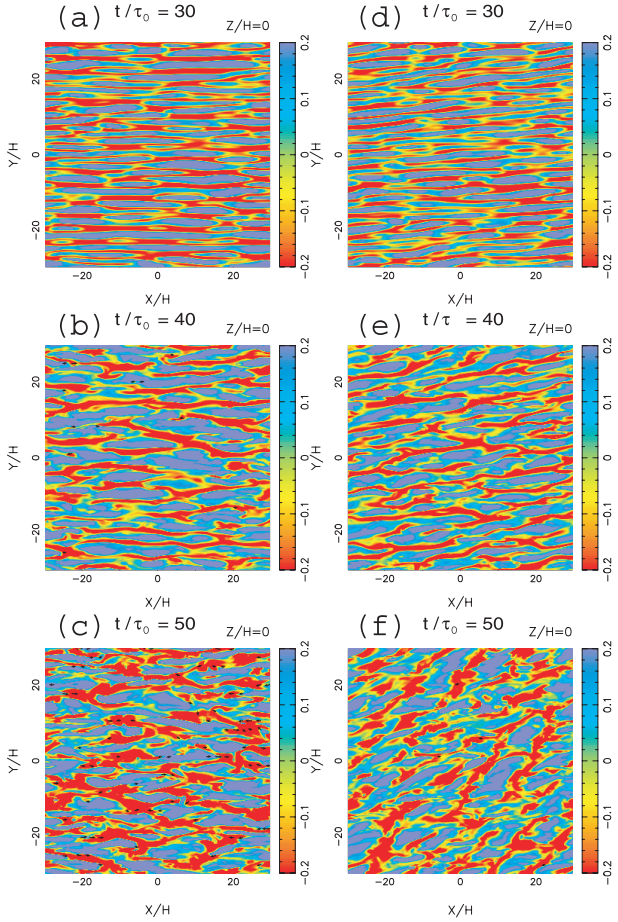

Fig. 12. Nonlinear simulation results for the no-magnetic shear mode (left; a, b, c: model 4) and for the magnetic shear mode (right; d, e, f: model 5), where a random-noise perturbation is initially assumed. These figures show a distribution of V_z on the photosphere surface ($z = 0H$) at $t/\tau_0 = 30$, 40, and 50.

- When there is no magnetic shear, the magnetic flux cannot rise as a whole (i.e., as a global or thick magnetic loop), but rises as fragmented flux tubes because of the interchange instability. In this case, the flux tubes expand significantly in the horizontal direction, so that the average magnetic pressure decreases greatly and hence the tube soon stops at a low height. However, when there is magnetic shear, the interchange mode is stabilized (see the Appendix for a linear stability analysis), so that the tube can rise as a whole and hence the height of the loop increases (see figure 15). For the same reason, the loop height increases with the shear angle or k_y.

4.2. *Discussion*

Shibata et al. (1989a) and other studies have shown that in 2D calculations the emerging magnetic flux rises into the corona with a density given by $\rho \propto z^{-4}$ and a magnetic field given by $B_x \propto z^{-1}$, due to a potential magnetic field. In the momentum equation, the gravity term, $\rho g \sim z^{-4}$, is smaller than the magnetic term, $B^2/dz \sim z^{-3}$, and therefore the expansion of the magnetic loops does not stop in the 2D model.

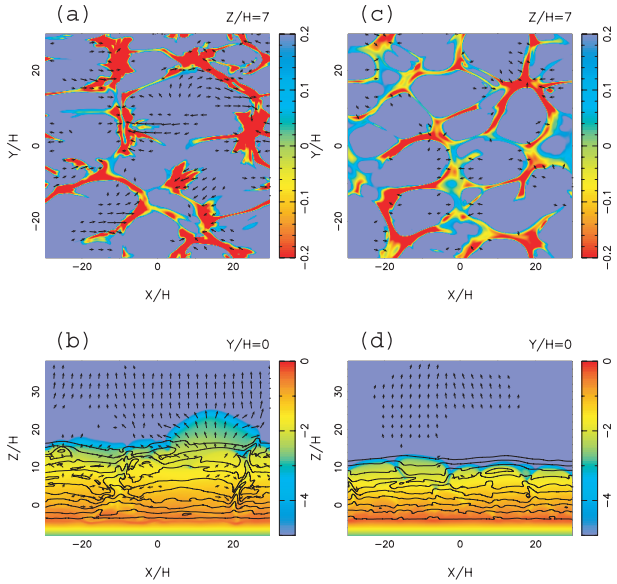

Fig. 13. Nonlinear simulation results at $t/\tau_0 = 50$ for the no-shear mode (left) and for the magnetic shear mode (right), where a random noise perturbation is initially assumed (model 4 and model 5). The upper figures show the distribution of V_z on the upper photosphere surface ($z = 7H$) and the lower figures show the magnetic field (colors), velocity field (vectors) and density (contour lines) on the $x-y$ surface.

When an initial periodic perturbation is assumed, the emerging flux rises into the corona and the magnetic field expands like a potential field. This special case is similar to model 10 of Matsumoto et al. (1993), where initially straight magnetic tubes are placed side by side. Because the emergence of each tube occurs at the same time, the expansions are blocked in the horizontal direction by each other and hence they rise in the vertical direction. In this case the emerging loop structure is similar to the 2D case (see figure 17a).

This result explains why a twisted magnetic tube rises into the corona in the studies of Magara and Longcope (2003) and Fan and Gibson (2004). The tube is twisted very strongly. Because the interchange instability occurs on the surface of the tube, the flux tube expands both horizontally and vertically. The horizontal expansion is blocked on both sides by other emerging fluxes. However, after the photosphere is full of magnetic field, the flux emerges from the upper photosphere to the corona in a realistic simulation of the solar atmosphere (see figure 13b). The critical wavelength λ_c in the photosphere is estimated to be

$$\lambda_c \sim 2\pi H \left(1 + \frac{1}{\beta}\right). \tag{18}$$

When $\beta = 0.5$, we find $\lambda_c \sim 18H$. In fact, figure 13b shows that the wavelength of the emerging flux into the corona is roughly $\sim 18H$, in agreement with the above estimate. As an initial localized perturbation is assumed, the emerging flux expands in the photosphere (see figure 17b). When an initial random perturbation is also assumed, the top of each loop of the emerging flux is different and the magnetic loop expands horizontally, like the growth of the localized perturbation loop (see figure 17c).

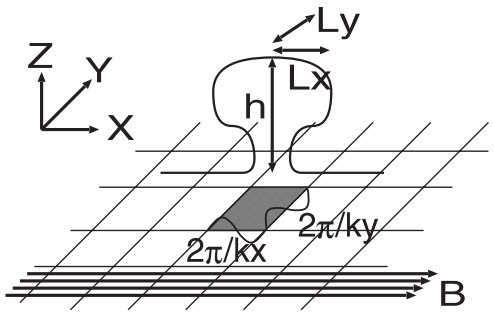

Fig. 14. Definitions of h, L_x, and L_y in a loop.

In figure 18 at $t = 15$–20 min, the expansion velocity in the horizontal direction is 10–15 km s^{-1} and the magnetic field strength is ~ 10 gauss. This velocity is estimated by assuming that the kinetic energy is equal to the magnetic energy, $\rho v^2 \sim B^2/(8\pi)$. Where $\rho \sim p/C_s^2$ and $v^2 \sim B^2/(8\pi p/C_s^2) = C_s^2/\beta$. If $\beta = 1$, $v \sim 1C_s = 10$ km s^{-1}. Although this velocity is large compared to the observed typical value for the photosphere, the expansion time-scale is very short ($\simeq 5$ min, see figure 18b) and the size is small ($\simeq 4000$ km). Therefore such phenomena may be observed by the high resolution La Palma, Swedish Vacuum Solar Telescope (De Pontieu et al. 2004). Future observations, using Solar-B for example, will reveal the detailed features of the emerging flux.

The author would like to thank Prof. K. Shibata and all the members of Kwasan Observatory, Kyoto University for fruitful discussions and help. The author is also grateful to Dr. D. Brooks for his careful reading of the manuscript and many valuable comments. This work was carried out by the joint research program of the Solar-Terrestrial Environment Laboratory, Nagoya University. This work was supported in part by the JSPS Japan-UK Cooperation Science Program (principal investigators: K. Shibata and N. O. Weiss).

Appendix. Linear Stability Theory and Comparison with Nonlinear Simulation

A.1. Linear Theory

In order to study the main characteristics of the linear instability of the magnetic flux sheet with magnetic shear, we analyze the linear stability of the flux sheet with a normal-mode method similar to that of Horiuchi et al. (1988). We consider the growth of a small perturbation that has a functional form $\delta W \propto \exp(i\omega t + ik_x x + ik_y y)$, where W is the physical quantity (ρ, p, v, $\boldsymbol{B}$), and δW is its perturbation. The linearized equations are the same as those in Horiuchi et al. (1988) and Nozawa et al. (1992) and the eigenvalue (ω) and eigenfunction are calculated numerically.

Figure 19 shows the growth rates $i\omega$ as a function of horizontal wave number $kH = H\sqrt{(k_x^2 + k_y^2)}$ for two cases, (a) the no-shear mode and (b) the shear mode, when $\beta_* = 1$, $\gamma = 1.05$, $D = 4H$, $z_{\min} = -8H$, $z_0 = -4H$, $z_{\rm cor} = 13H$, and $T_{\rm cor}/T_{\rm ph} = 25$. The numbers attached to each curve indicate the ratio k_y/k_x. When the wavenumber along the field line (k_x) is fixed, the growth rate increases with the perpendicular wavenumber, k_y. Thus, a perturbation with a shorter wavelength perpendicular to the magnetic field line grows faster than perturbations with longer wavelengths.

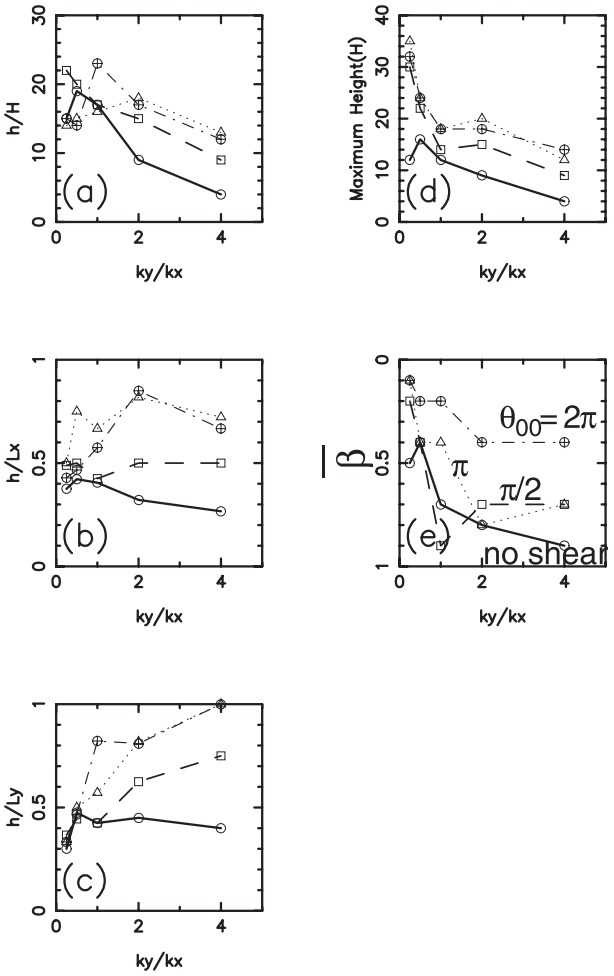

Fig. 15. Normalized loop height (a, b, c: h/H, h/L_x, h/L_y) as a function of k_y/k_x at $t/\tau_0 = 55$ for a localized perturbation. The numbers indicate the shear angle, θ_{00} (radian). Here, h is the height of the emerging flux loop, L_x the half length of the loop, and L_y the width of the loop (see figure 14). Also shown are (d) the maximum heights of the loop and (e) the values of the averaged plasma β (see figure 11f).

The linear growth rate of the non-sinusoidal perturbations (14) is the same as that of the sinusoidal perturbations (single plane wave) in the shear mode because the non-sinusoidal perturbation can be decomposed into two plane wave perturbations whose wave vectors are (k_x, k_y) and $(k_x, -k_y)$.

Since the perturbations are added in the direction parallel to the magnetic field on the top surface of the flux sheet, the Parker mode dominates at long wavelengths ($k_y/k_x = 0$), where the linear analytic growth rate has a relative maximum value $iw \sim 0.124$ at $kH = 0.275$ ($\lambda = 23H$).

When $k_y/k_x = 0$, the growth rate is larger for the no-shear mode (a) than that for the shear mode (b). This is because the interchange mode is coupled in (b), even for $k_y = 0$, since there is a layer where $k_x \perp \boldsymbol{B}$ in the sheared flux sheet.

On the other hand, the growth rate is generally smaller in (b)

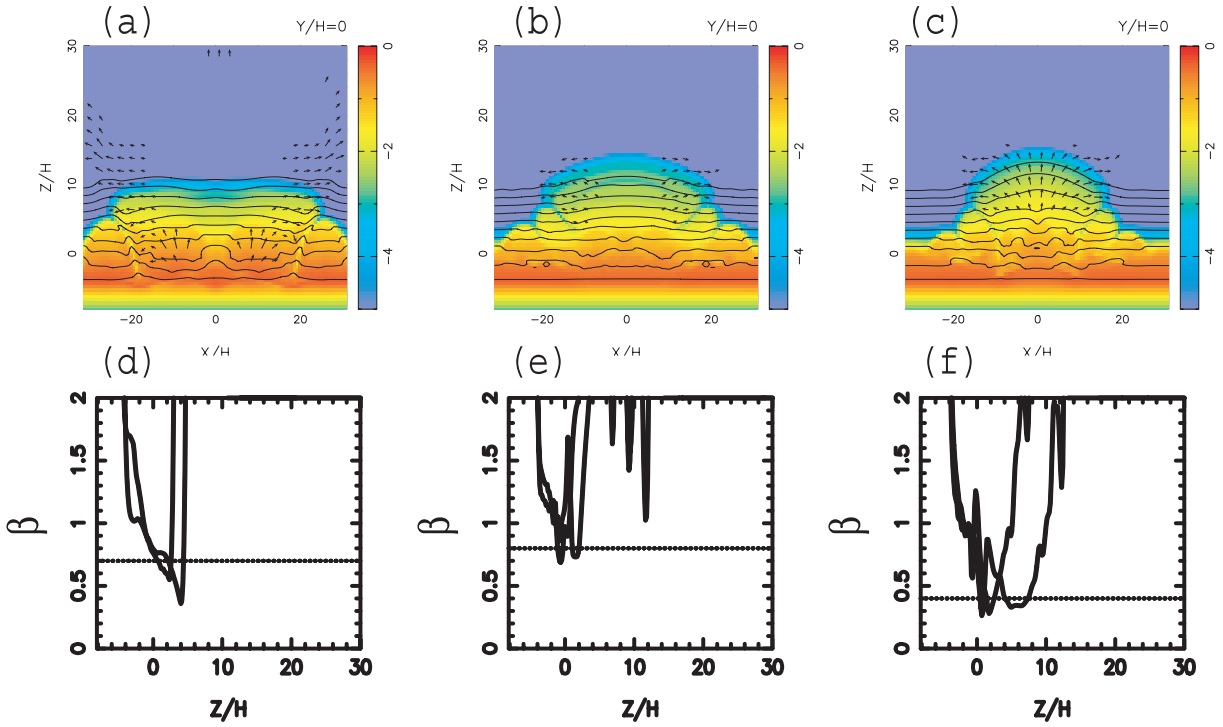

Fig. 16. Nonlinear simulation results for shear angles of $\theta_{00} = 0$ (left; a, d) at $t/\tau_0 = 50$, π (middle; b, e) at $t/\tau_0 = 55$, and 2π (right; c, f) at $t/\tau_0 = 55$ when $k_y/k_x = 2$ (models 6, 7 and 8) for (a, b, c) the x–y surface (see figure 6d) and (d, e, f) the plasma β distribution in z at $(x, y) = (0H, 0H)$ (see figure 8f).

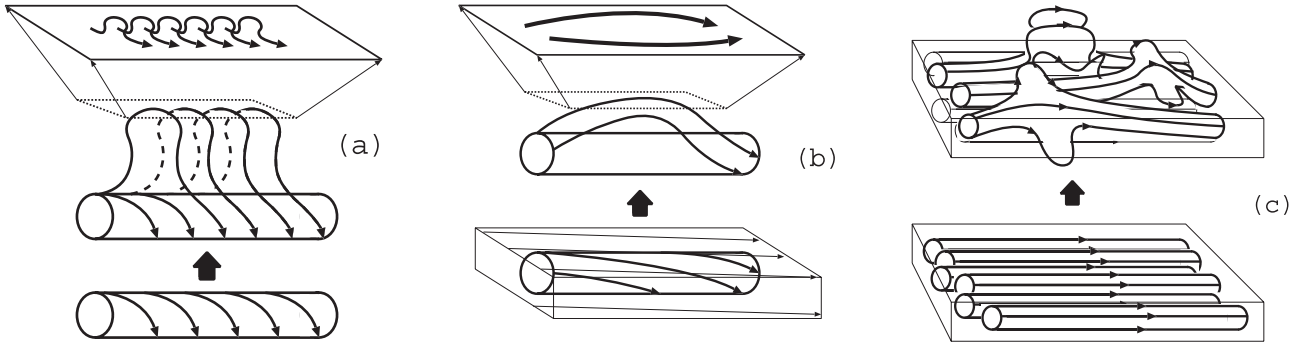

Fig. 17. Schematic pictures of emergence in (a) strong twisted flux tube, (b) weak twisted flux tube or magnetic flux sheet, and (c) random perturbation with no magnetic shear.

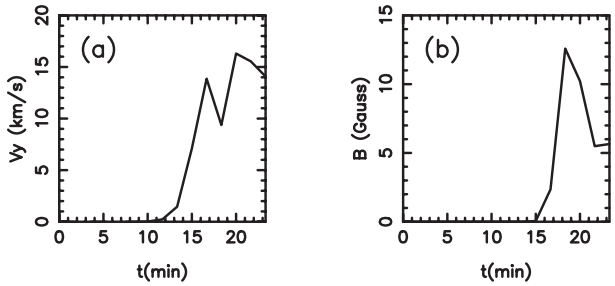

Fig. 18. Time evolution of the y-component of the velocity and magnetic strength at $x = 0H$, $y = 10H$, $z = 5H$ for model 2.

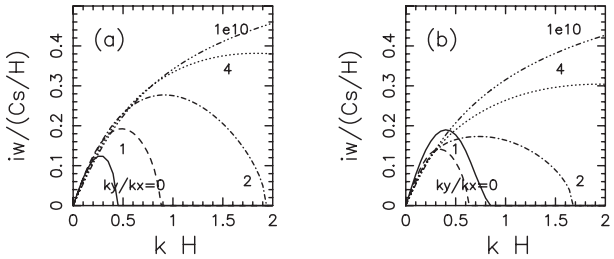

Fig. 19. Normalized growth rate (in units of C_s/H) as a function of k ($kH = \sqrt{k_x^2 + k_y^2}\,H$) for $k_y/k_x = 0$, 1, 2, 4, and ∞ (1.0e10) for (a) the no-shear mode and (b) the magnetic shear mode. $\beta_* = 1.0$ and $\gamma = 1.05$ are assumed.

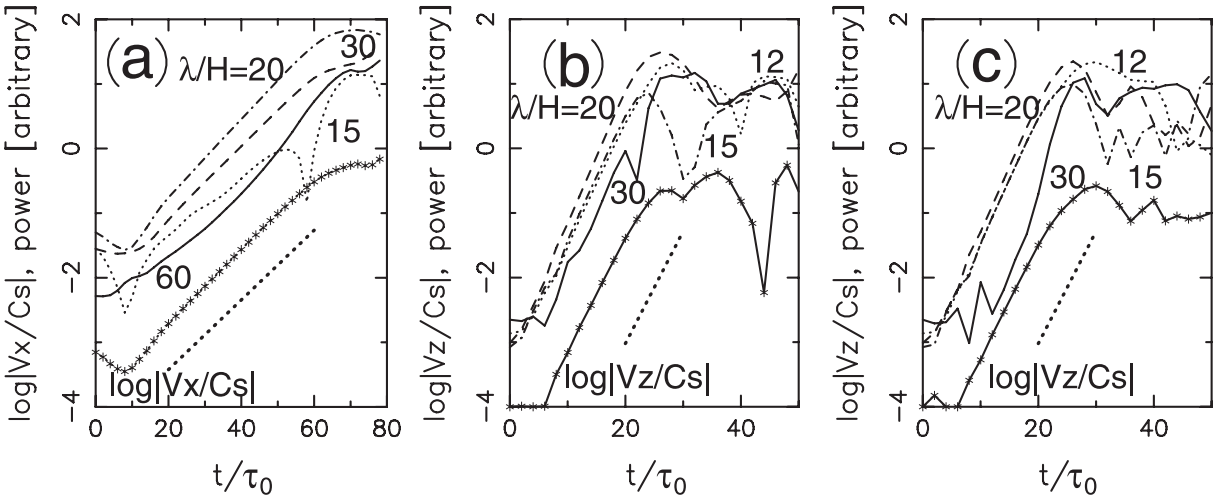

Fig. 20. Time evolutions of the x-component of the velocity at $z = 0$ for models 1, 4, and 5. (a) Mode analysis and time evolution of $\log|V_x|$. The full line is $\lambda = 60H$ ($k' = 1$, $kH = 0.10$), the dashed line $k' = 2$ ($\lambda = 30H$, $kH = 0.21$), the dot-dashed line $k' = 3$ ($\lambda = 20H$, $kH = 0.31$), the dotted line $k' = 4$ ($\lambda = 15H$, $kH = 0.42$), and the full line with $*$ the time evolution of $\log|V_x/C_s|$ at the point $(x, y, z) = (0, 0, 0)$. The dotted line represents the growth rate obtained from linear stability analysis ($i\omega = 0.124$) for $\lambda = 20H$ ($k' = 3$, $kH = 0.314$). Also shown are (b) the no-shear mode and (c) the shear mode of $\log|V_z|$, with the meanings of the lines being the same as in (a).

than in (a) for short wavelengths. This is because the interchange mode tends to be stabilized by the magnetic tension force in the sheared magnetic field.

Therefore, for the shear mode (b), the maximum growth rate of $k_y/k_x = 0$ is larger than that of $k_y/k_x = 1, 2$, as the bottom of the sheet is unstable because $k_x \perp \boldsymbol{B}$.

With $\boldsymbol{B} = 0$ and $k_y/k_x = 10^{10}$ for the no-shear mode, the growth rate does not have a maximum and increases monotonically with the wavenumber. The growth rate in this case is the same as the pure Rayleigh–Taylor instability, which is $a_m\sqrt{kg}$. Here, a_m is a parameter of the magnetic interchange instability, and has a value of 0.33.

A.2. 2D and 3D Nonlinear Simulations with Single or Random Perturbations

The horizontal wavelength ($\lambda/H = 20$) of the initial perturbation is close to the wavelength of the maximum growth rate for $\beta = 1$; the growth rate is 0.12 (see the thick dotted line in figure 20a). Since the perturbation given in the initial condition is not an eigenfunction, the most unstable wavelength does not grow, but other modes are excited by the nonlinear effect. The above results show that the instability grows on the wavelength given in the initial conditions in the 2D case.

Figures 20b, c show the results for a random initial perturbation for both the no-shear and shear modes. It is found that the growth rate in this case is 0.4. Comparing this value with linear theory, we find the corresponding wavenumber is $kH = 1.7$ ($\lambda = 3.7H$) for $k_y/k_x = \infty$. This $\lambda = 3.7H$ is consistent with $18 \times \Delta x$ ($= \Delta y = 0.2H$), which agrees with the maximum wavelength resolution of the numerical scheme.

References

Baierlein, R. 1983, MNRAS, 205, 669
Basu, S., Mouschovias, T. Ch., & Paleologou, E. V. 1997, ApJ, 480, L55
Cattaneo, F., Chiueh, T., & Hughes, D. W. 1990, Journal of Fluid Mechanics, 219, 1
Chou, W., Tajima, T., Matsumoto, R., & Shibata, K. 1999, PASJ, 51, 103
De Pontieu, B., Erdélyi, R., & James, S. P. 2004, Nature, 430, 536
Fan, Y. 2001, ApJ, 554, L111
Fan, Y., & Gibson, S. E. 2004, ApJ, 609, 1123
Hachisu, I., Matsuda, T., Nomoto, K., & Shigeyama, T. 1992, ApJ, 390, 230
Hanawa, T., Matsumoto, R., & Shibata, K. 1992, ApJ, 393, L71
Hanasz, M., Otmianowska-Mazur, K., & Lesch, H. 2002, A&A, 386, 347
Horiuchi, T., Matsumoto, R., Hanawa,T., & Shibata, K. 1988, PASJ, 40, 147
Hughes, D. W., & Proctor, M. R. E. 1988, Annual Review of Fluid Mechanics, 20, 187
Ishii, T. T., Kurokawa, H., & Takeuchi, T. T. 1998, ApJ, 499, 898
Kamaya, H., Mineshige, S., Shibata, K., & Matsumoto, R. 1996, ApJ, 458, L25
Kim, J., Franco, J., Hong, S. S., Santillán, A., & Martos, M. A. 2000, ApJ, 531, 873
Kim, J., Hong, S. S., Ryu, D., & Jones, T. W. 1998, ApJ, 506, L139
Kim, J., Ryu, D., & Jones, T. W. 2001, ApJ, 557, 464
Kim, W., Ostriker, E. C., & Stone, J. M. 2002, ApJ, 581, 1080
Kruskal, M. D., & Schwarzchild, M. 1954, Proc. R. Soc. London, Ser. A, 223, 348
Kurokawa, H. 1989, Space Science Reviews, 51, 49

Kurokawa, H., Wang, T., & Ishii, T. T. 2002, ApJ, 572, 598
Kusano, K., Moriyama, K., & Miyoshi, T. 1998, Physics of Plasmas, 5, 2582
Magara, T. 2004, ApJ, 605, 480
Magara, T., & Longcope, D. W. 2001, ApJ, 559, L55
Magara, T., & Longcope, D. W. 2003, ApJ, 586, 630
Matsumoto, R., Horiuchi, T., Shibata, K., & Hanawa, T. 1988, PASJ, 40, 171
Matsumoto, R., & Shibata, K. 1992, PASJ, 44, 167
Matsumoto, R., Tajima, T., Chou, W., Okubo, A., & Shibata, K. 1998, ApJ, 493, L43
Matsumoto, R., Tajima, T., Shibata, K., & Kaisig, M. 1993, ApJ, 414, 357
Matthews, P. C., Hughes, D. W., & Proctor, M. R. E. 1995, ApJ, 448, 938
Nozawa, S., Shibata, K., Matsumoto, R., Sterling, A. C., Tajima, T., Uchida, Y., Ferrari, A., & Rosner, R. 1992, ApJS, 78, 267
Parker, E. N. 1955, ApJ, 121, 491
Parker, E. N. 1966, ApJ, 145, 811
Parker, E. N. 1979, Cosmical Magnetic Fields (Oxford: Clarendon Press)
Ritchmyer, R. D., & Morton, K. W. 1967, Difference Methods for Initial-Value Problems, 2nd ed. (New York: Interscience)
Rubin, E. L., & Burstein, S. Z. 1967, J. Comp. Phys., 2, 178
Ryu, D., Kim, J., Hong, S. S., & Jones, T. W. 2003, ApJ, 589, 338
Shibata, K. 1983, PASJ, 35, 263
Shibata, K., & Matsumoto, R. 1991, Nature, 353, 633
Shibata, K., Nozawa, S., Matsumoto, R., Sterling, A. C., & Tajima, T. 1990a, ApJ, 351, L25
Shibata, K., Tajima, T., & Matsumoto, R. 1990b, ApJ, 350, 295
Shibata, K., Tajima, T., Matsumoto, R., Horiuchi, T., Hanawa, T., Rosner, R., & Uchida, Y. 1989a, ApJ, 338, 471
Shibata, K., Tajima, T., Steinolfson, R. S., & Matsumoto, R. 1989b, ApJ, 345, 584
Spruit, H. C. 1974, Sol. Phys., 34, 277
Spruit, H. C., Nordlund, A., & Title, A. M. 1990, ARA&A, 28, 263
Tajima, T., & Shibata, K. 1997, Plasma Astrophysics (Reading, Massachusetts: Addison-Wesley)
Zwaan, C. 1985, Sol. Phys., 100, 397
Zwaan, C. 1987, ARA&A, 25, 83